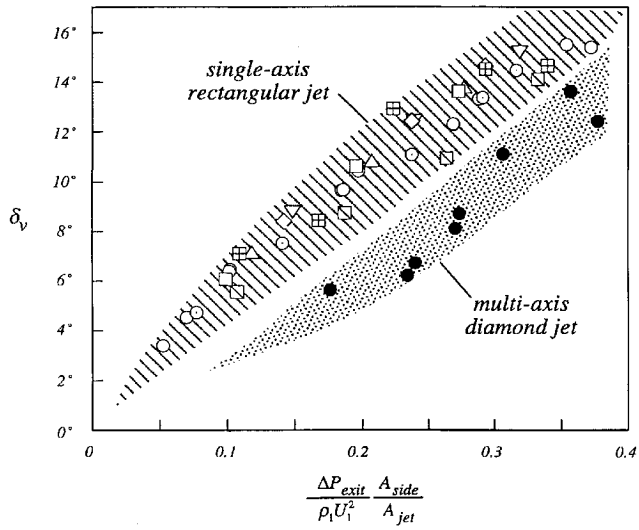


**Fig. 3 Thrust vector response curves for Mach 2 jets.**

the single-axis CFTV results and includes data for hot and cold jets measured over a range of collar design parameters, i.e., various collar lengths and suction gap heights. Estimates of $\delta_v$ for the single-axis study were obtained using a control volume analysis including integrated pressure profiles measured along the collar surface as well as flow visualization images using the PLS technique employed in the present study. Within experimental uncertainty, the single-axis data essentially collapse onto a single curve displaying an approximately linear dependence on the nondimensional pressure parameter. The good collapse of the single-axis thrust vector data over a wide parametric range indicates that the scaling in Fig. 3 captures the essential features of the pressure forces and momentum fluxes contained in a complete control volume analysis applied to the jet-nozzle system. Furthermore, the agreement between the vectoring angles obtained using a control volume analysis and those estimated using PLS images indicates the reliability of optical techniques for measuring $\delta_v$.

The data for the current multiaxis study are shown in the lower curve, where the scatter and the uncertainty in the measurements are roughly indicated by the shaded region. As in the single-axis study, the jet thrust vector angle is almost linearly proportional to the amount of counterflow. At the maximum suction pressure of approximately 7.5 psia—a pressure limitation primarily imposed by the efficiency of the vacuum system—a maximum deflection angle of approximately 15 deg was obtained. The mass flux rates of the counterflowing stream were too low to be accurately measured in the present study. However, similar meaurements made in the Mach 2 rectangular jet[4] suggest that the counterflow mass flux is well below 2% of the primary jet flow for all cases shown in Fig. 3.

Although the multiaxis data show reasonably linear behavior, similar to the performance of a single-axis system, the curves for the two cases are distinct and the single-axis geometry appears to be slightly more efficient. We believe that the primary reason for the differences in thrust vector performance of the single- and multiaxis systems is attributable to a noticeable leakage between adjacent chambers of the collar assembly of the diamond jet. This was determined by monitoring the static-pressure distributions in the four chamber of the dimond nozzle. Leakage effects indicate that counterflow is not confined to a single shear layer of the diamond jet, resulting in a degradation of performance principally attributable to the transverse pressure gradient across the shear layer. Although these three-dimensional effects undoubtedly will influence the collar performance, we believe that they can be minimized by improvements in collar design. The collar design was not optimized in the present study, where the goal was to demonstrate the proof of concept of a multiaxis thrust vector system based on fluidic control.

## Conclusions

Fluidic thrust vector control was examined in a Mach 2 diamond nozzle to determine the efficacy of multiaxis control using counterflow. The results clearly demonstrate that a secondary counterflowing stream applied along the periphery of the primary shear layer can be used effectively to achieve nonhysteretic thrust vector control in multiaxes and up to angles approaching 15 deg. These results are an extension of previous studies where CFTV was applied to single-axis pitch control at Mach numbers up to 2 and indicate the robustness of the CFTV concept, which has many attractive features including the elimination of mechanical control surfaces and the inherent film cooling made possible by the ambient counterflow.

## Acknowledgments

Support for this research was provided by the U.S. Office of Naval Research (Contract N00014-92-J-1406) and NASA (Contract NAG-2930).

## References

[1]Snow, B. H., "Thrust Vectoring Control Concepts and Issues," Society of Automotive Engineers TP Ser. 901848, 1990.

[2]Capone, F., Smereczniak, P., Spetnagel, D., and Thayer, E., "Comparative Investigation of Multiplane Thrust Vectoring Nozzles," AIAA Paper 92-3264, July 1992.

[3]Warren, R. W., "Some Parameters Affecting the Design of Bistable Fluid Amplifiers," ASME Symposium on Fluid Jet Control Devices, Winter Annual Meeting, American Society of Mechanical Engineers, Nov. 1962, pp. 75–82.

[4]Strykowski, P. J., Krothapalli, A., and Forliti, D. J., "Counterflow Thrust Vectoring of Supersonic Jets," AIAA Paper 96-0115, Jan. 1996; also, *AIAA Journal* (submitted for publication).

[5]Alvi, F. S., Krothapalli, A., Washington, D., and King, C. J., "Aeroacoustic Properties of a Supersonic Diamond-Shaped Jet," *AIAA Journal*, Vol. 34, No. 8, 1996, pp. 1562–1569.

# Three-Dimensional Velocity Measurements Within Görtler Vortices

J. A. Rothenflue* and P. I. King†
*U.S. Air Force Institute of Technology, Wright–Patterson Air Force Base, Ohio 45433*

## Introduction

IN 1940, Görtler[1] predicted that streamwise-oriented, counter-rotating vortices would develop in response to the centrifugal instability within a laminar boundary layer over a concave surface. Hot-wire[2] and laser Doppler[3] anemometry (LDA) have been used to detect Görtler vortices (GVs) through spanwise periodic variations in the streamwise velocity component within the boundary layer; however, cross-stream velocity component measurements within the vortices have remained conspicuously absent from the literature.

Obtaining cross-stream velocity measurements within GVs is difficult because of the weak nature of the disturbance. A GV in a laminar boundary layer is, in reality, little more than a small twist of the fluid, typically turning through no more than 90 deg before breakup as a result of boundary-layer transition to turbulence.[4] A coordinate system and geometry for a typical set of GVs are depicted in Fig. 1, where $R$ is the radius of curvature of the surface, $\delta$ is the boundary-layer thickness, and $U$ is the freestream velocity.[5] The $u$, $v$, and $w$ velocity components are the local flow velocities in the $x$, $y$, and $z$ directions, respectively.

Received Jan. 6, 1995; revision received Jan. 2, 1996; accepted for publication April 15, 1996. This paper is declared a work of the U.S. Government and is not subject to copyright protection in the United States.

*Doctoral Candidate; currently Deputy for Technology Transfer, Applied Laser Technology Branch, U.S. Air Force Phillips Laboratory, 3550 Aberdeen Avenue, SE Building 619, Kirtland Air Force Base, NM 87117-5776. Member AIAA.

†Associate Professor, Department of Aeronautics and Astronautics, 2950 P Street. Senior Member AIAA.

GVs will induce spanwise periodic variations in all three velocity components within a boundary layer. This phenomenon is illustrated in Fig. 2, for an arbitrary spanwise periodic function. One theoretical treatment[4] assumes these velocity disturbances are sinusoidal with wavelength independent of $x$. The $u$ variations occur with ascent of low-speed fluid in the upwash regions and descent of higher-speed fluid in the downwash regions. The $v$ and $w$ variations result from the flow vorticity, with 180- and 90-deg phase shifts, respectively, relative to the $u$ profile. Magnitudes of the $u$, $v$, and $w$ fluctuations vary with height above the solid boundary.

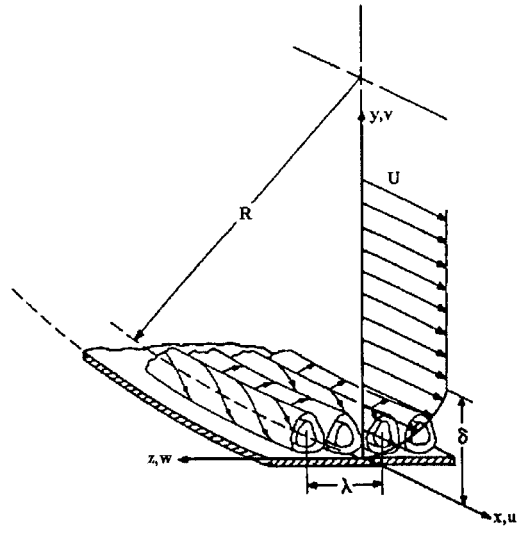


**Fig. 1 Coordinate system and GV geometry.**

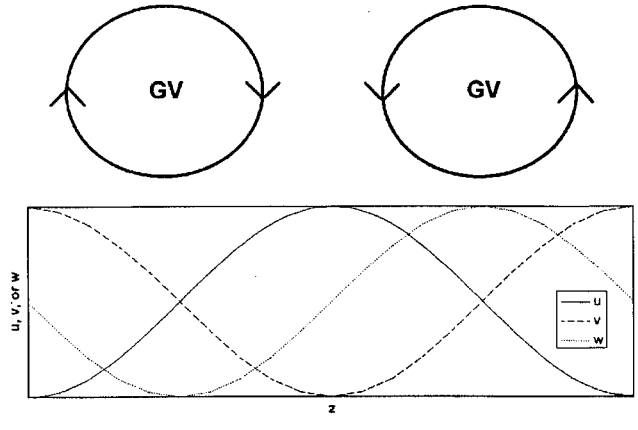


**Fig. 2 Velocity variations within GVs.**

For this research, three-component LDA recorded spanwise periodic variations of all three velocity components within GVs, and a four-degree-of-freedom, least-squares, sine wave curvefit was employed to obtain estimates for oscillation amplitude and GV wavelength. The curvefit wavelengths derived from all velocity components exhibit a scatter of approximately 10%, with $v$ and $w$ oscillation amplitudes approximately one order of magnitude smaller than the $u$ oscillation amplitude.

## Test Setup and Procedure

The concave test surface for this research has a radius of curvature of 1 m and bends through 90 deg. It is enclosed in a curved channel with movable inner wall, to allow a zero streamwise pressure gradient to be established over the length of the concave surface, and the leading edge of the test surface is located at the beginning of channel curvature. The gap between the test surface and test section inner wall was nominally 8 cm. The freestream turbulence intensity of the air entering the test section, given by $Tu = [(u_{\text{rms}}^2 + v_{\text{rms}}^2 + w_{\text{rms}}^2)/3] \times (1/U)$, was approximately 1.0%. No high-pass filtering of the velocity data was employed in the turbulence calculation.

The requirement to obtain nonintrusive, simultaneous measurements of all three velocity components very near the test surface prohibited the use of a physical probe. Thus, a three-dimensional LDA system was used that included a 300-mW argon laser, 600-mm focal length optics, and three DANTEC Burst Spectrum Analyzers (BSAs) controlled by a desktop computer running DANTEC Burstware, version 3.0. Off-axis backscatter measurements were performed, and the lasers were aligned so that the ellipsoidal probe volume measured approximately 150 × 150 × 215 $\mu$m.

To resolve the small cross-stream components, the error in the measured mean velocities was minimized by maximizing the number of particles detected by the LDA apparatus. First, to maximize the time available for data acquisition, a mass regulator valve controlled the delivery of air to the test section, thus minimizing fluctuations in the freestream velocity (variations were less than 1% during a test) that would alter GV geometry. Second, to increase the LDA's ability to detect the particles in the flow, the angle between the two laser probes was maximized within the physical limitations of the optical bench (70 deg), minimizing interference from the beams' reflection from the wall. Finally, for increased accuracy, velocities were calculated from the residence-time-weighted mean of a large number of particles (2000) for all measurements.

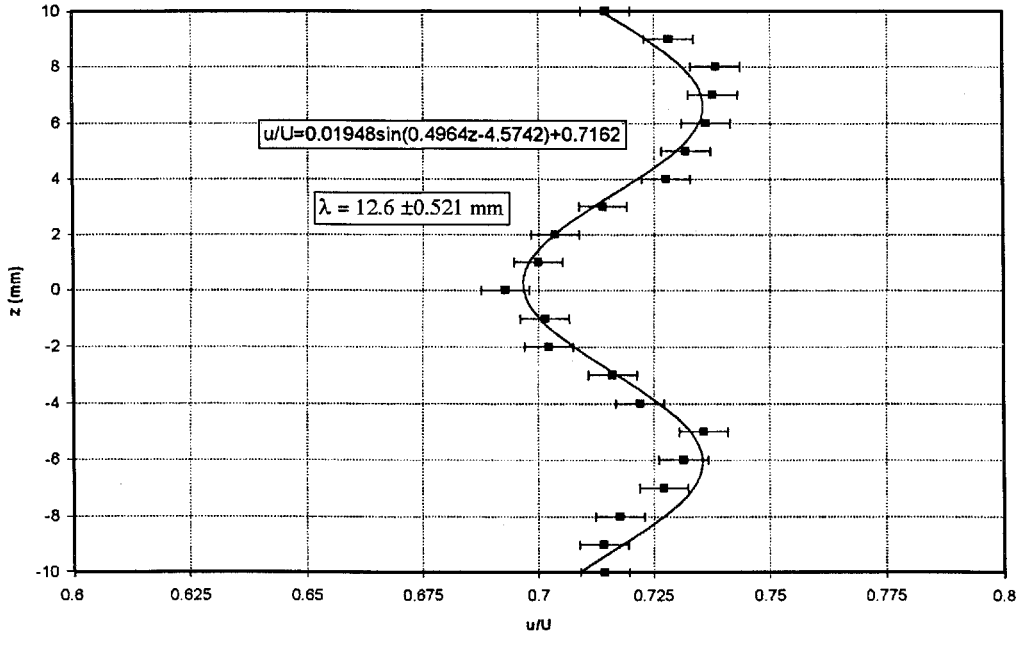


**Fig. 3 Spanwise $u$ profile; $U$ = 3.6 m/s, $x$ = 400 mm, and $y$ = 3.0 mm.**

## Results

To detect the velocity variations illustrated in Fig. 2, spanwise profiles were taken at a $y/\delta = 0.143$ and 0.429. The lower station maximized the ability to detect the $w$ variation near the wall, whereas the upper station allowed detection of the $u$ and $v$ variations, which are larger away from the wall. Measurements were taken at an $x$ location 400 mm from the test plate leading edge under the following conditions: $U = 3.6$ m/s, $\delta = 7.0$ mm, and $Re_x = 9.0 \times 10^4$. The Görtler number $G$ indicates the relative influences of centrifugal and viscous forces on fluid particle motion, where $G = (U\delta_r/\nu)(\delta_r/R)^{1/2}$ and $\delta_r = (\nu x/U)^{1/2}$. Although theoretical approaches to the Görtler problem allow for various minimum values of $G$ to denote centrifugal instability of the boundary layer, $G > 1$ generally implies that the boundary layer is unstable. For the given test conditions, $G = 11.0$, indicating the expectation of GV development.

Measured spanwise $u$, $v$, and $w$ profiles are given in Figs. 3–5, respectively. The error bars and estimated wavelength ranges in the figures are 90% confidence intervals. Wavelength estimates from the curvefits range from 12.7 to 14.1 mm, and the linear unbiased minimum-variance estimate of GV wavelength from these three curves is $\lambda = 13.2$ mm. A nondimensional GV wavelength parameter is $\Lambda = (U\lambda/\nu)(\lambda/R)^{1/2}$. In the absence of strong freestream disturbances, Görtler theory[5] would suggest that when GV development occurs ($G > 1$), $150 < \Lambda < 500$. For this case, $\Lambda = 332$, in good agreement with predictions. Also note that phase shifts of the $v$ and $w$ profiles relative to the $u$ profile are consistent with the model presented in Fig. 2.

As mentioned earlier, the $w$ variation was detectable only near the wall ($y/\delta = 0.143$), whereas $u$ and $v$ variations were detectable farther away from the wall ($y/\delta = 0.429$). At either station, however, the amplitude of the $v$ or $w$ oscillations was approximately one order of magnitude smaller than the $u$ oscillation amplitude.

Not shown here are results for $U = 7.5$ and 15.0 m/s (with wavelengths corresponding to $\Lambda = 367$ and 359, respectively). In both cases, the relative phase shifts and oscillation amplitudes of the periodic data for all three velocity components were as for the $U = 3.6$ m/s case. In addition, for any other $x$ locations on the plate,

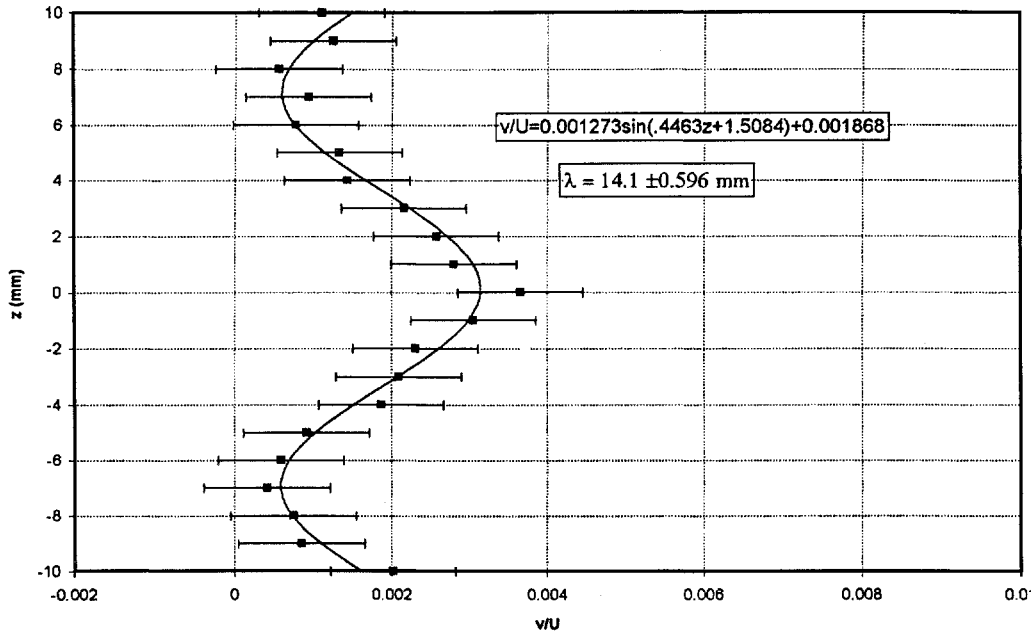


**Fig. 4 Spanwise $v$ profile; $U = 3.6$ m/s, $x = 400$ mm, and $y = 3.0$ mm.**

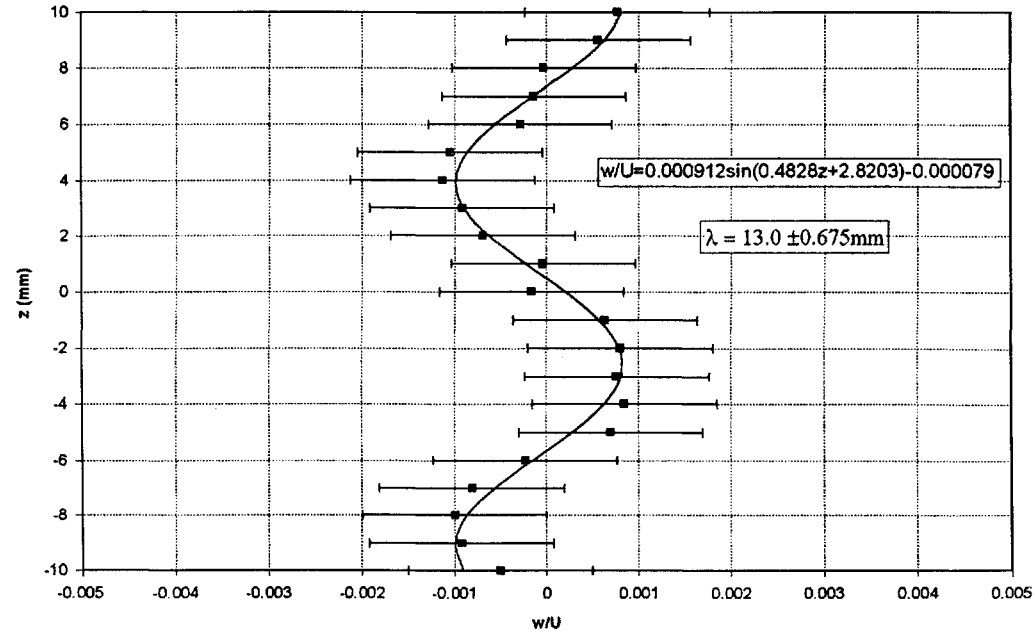


**Fig. 5 Spanwise $w$ profile; $U = 3.6$ m/s, $x = 400$ mm, and $y = 1.0$ mm.**

no significant streamwise variation in GV wavelength occurred for any of the three freestream velocities.

## Conclusions

Spanwise varying velocity components within GVs were obtained with a three-dimensional LDA. The $w$ disturbance was only detectable near the wall ($y/\delta = 0.143$), whereas the $u$ and $v$ disturbances were detectable higher up in the boundary layer ($y/\delta = 0.429$). The data were well correlated with sinusoidal variations, and the estimated vortex wavelength from these measurements matched theoretical expectations. Measurements taken at other freestream velocities and $x$ locations indicated streamwise conservation of GV wavelength.

## References

[1]Görtler, H., "On the Three-Dimensional Instability of Laminar Boundary Layers on Concave Walls," NACA TM 1375, June 1954 (English translation).

[2]McCormack, P. D., Welker, H., and Kelleher, M., "Taylor-Goertler Vortices and Their Effect on Heat Transfer," *Journal of Heat Transfer*, Vol. 102, No. 1, 1970, pp. 101–112.

[3]Winoto, S. H., Durão, D. F. G., and Crane, R. I., "Measurements Within Görtler Vortices," *Journal of Fluids Engineering*, Vol. 101, 1979, pp. 517–520.

[4]Floryan, J. M., "On the Görtler Instability of Boundary Layers," National Aerospace Lab., TR-1120T, Tokyo, Japan, Aug. 1991.

[5]White, F. M., *Viscous Fluid Flow*, 2nd ed., McGraw–Hill, New York, 1991, p. 368.

# Navier–Stokes Simulation of a Cone-Derived Waverider with Multidirectional Curvature

Sheam-Chyun Lin* and Ming-Chiou Shen†
*National Taiwan Institute of Technology, Taipei, Taiwan 10772, Republic of China*

## Introduction

THE idea of using a waverider concept as the primary basis of designing a hypersonic vehicle has been considered seriously in the last decade. In 1980, Rasmussen[1] derived waveriders from the circular and elliptic cones by the perturbation method on the basis of hypersonic small-disturbance theory (HSDT), and then Rasmussen et al.[2] conducted an experiment proving that this analytic approximation is highly credible. Later, Lin and Rasmussen[3] extended the circular cone solution to include the transverse and longitudinal curvatures. Consequently, the waverider shapes with multidirectional curvature (MDCWR)[4] are created by using this solution. It was shown that the MDCWR has the advantage of efficient volumetric packaging and enhanced lift-to-drag ratio ($L/D$).

Recently, Liao et al.[5] simulated the flowfields for the elliptic-cone-derived waverider (ECDWR) of Rasmussen et al.[2] at both design and off-design flight conditions. They found that the shock wave still did not attach to the wing tip under the on-design conditions. Also, an obvious vortex occurred on the upper surface when the angle of attack increased to 5 deg. Until now, no numerical simulation for the MDCWR has been performed systematically. Therefore, the numerical simulation for the MDCWR is studied in this work. The analysis investigates both on-design Mach 4 and off-design conditions, including angles of attack from 0 to 10 deg and Mach numbers from 2 to 6. In addition, these numerical results are compared with the previous studies of the ECDWR.[5]

Received Nov. 1, 1995; presented as Paper 96-0313 at the AIAA 34th Aerospace Sciences Meeting, Reno, NV, Jan. 15–19, 1996; revision received April 1, 1996; accepted for publication April 7, 1996. 

*Associate Professor, Department of Mechanical Engineering. Member AIAA.

†Graduate Research Assistant, Department of Mechanical Engineering.

## Waverider Generation and Numerical Method

In this Note, a fourth-order freestream trailing-edge curve with zero-slope edge with the approximate analytic solution of Lin and Rasmussen[3] and Lin and Luo[4] is selected to generate the MDCWR. For comparison with previous investigations of the ECDWR, all design parameters and flight conditions except the longitudinal curvature are identical to those of the ECDWR reported by Rasmussen et al.[2] and Liao et al.[5] Also, the flow was considered laminar. Moreover, the inability to estimate viscous effect in HSDT is compensated by using an average skin-friction coefficient ($\bar{C}_f$), proposed by He and Rasmussen,[6] for comparing with the viscous numerical results.

The three-dimensional compressible Navier–Stokes equations are solved by using Roe's implicit, finite volume, upwind algorithm.[7] By means of the monotone upstream-centered schemes for conservation laws interpolation of the primitive variables, the quantity in the inviscid fluxes is obtained. Furthermore, the thin-layer approximation is utilized for each viscous direction to calculate the viscous flux terms by a second-order central difference. Moreover, the impermeable and adiabatic wall boundary conditions are imposed in the present calculations. The outer boundary and initial flow conditions are specified as freestream flow properties. In addition, a calorically perfect gas was assumed here. With regard to the grid generation, a Poisson's equation,[8] together with a nonlinear successive over-relaxation technique, is used to generate a full three-dimensional boundary-fitted grid in the convergence criterion that the maximum error for each iteration is less than $10^{-5}$. Here, two grid systems of $51 \times 106 \times 81$ (see Fig. 1) and $26 \times 54 \times 40$, which clustered near the shock layer, wall, apex, and wing tip of the MDCWR, are generated to test the grid independence.

## Results and Discussion

Before proceeding with the investigation of the waverider, two model problems are considered to validate the present numerical techniques, results of which are summarized in Table 1. The solutions of these model problems confirm that the numerical procedure does perform as expected.

**Table 1 Model problems**

| Case | $Re \times 10^6$ | $M_\infty$ | Grid size | Comparison | Error, % |
|---|---|---|---|---|---|
| Flat plate | 1.0 | 4.0 | $101 \times 101$ | Van Driest[9] | 0.12 |
| ECDWR | 3.94 | 4.0 | $41 \times 91 \times 51$ | Liao et al.[5] | 0.62 |

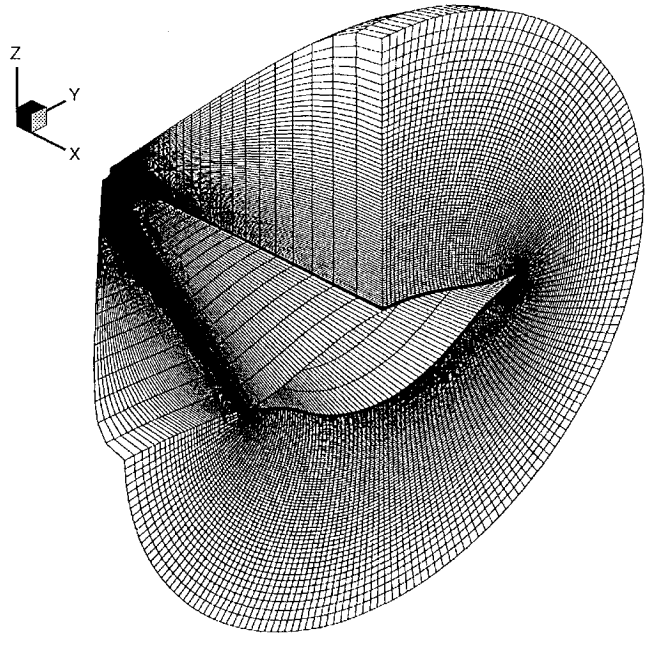


**Fig. 1 Three-dimensional grid for MDCWR ($51 \times 106 \times 81$).**